TDA Progress Report 42-108 February 15, 1992

Pointing-Error Simulations of the DSS-13 Antenna Due to Wind Disturbances

W. Gawronski
Ground Antennas and Facilities Engineering Section

B. Bienkiewicz
Civil Engineering Department
Colorado State University

R. E. Hill[1]

Accurate spacecraft tracking by the NASA DSN antennas must be assured during changing weather conditions. Wind disturbances are the main source of tracking errors. This article presents the development of a wind-force model and simulations of wind-induced pointing errors of DSN antennas. The antenna model includes the antenna structure, the elevation and azimuth servos, and the tracking controller. Simulation results show that pointing errors due to wind gusts are of the same order as errors due to static wind pressure and that these errors (similar to those of static wind pressure) satisfy the velocity quadratic law. The methodology presented is used for wind-disturbance estimation and for design of an antenna controller with wind-disturbance rejection properties.

I. Introduction

Reliable estimates of the pointing error due to wind disturbances are required for operating antennas as well as for designing effective controllers. There are two types of wind-induced pointing errors: steady-state error due to static wind pressure and dynamic error due to wind turbulence. Steady-state error models of antennas have been investigated by Katow and McGinness [1,2]; the dynamic error of the DSS-14 antenna has been analyzed by Massoudi [3]; and the 100-m NRAO antenna has been analyzed by Hill.[2]

[1] Independent consultant to the Ground Antennas and Facilities Engineering Section.

[2] R. Hill, "Servo Design Studies and Pointing Performance Analysis for a 100-m Aperture Radiotelescope," in *Servo Design Specification for the 100-meter Unblocked Aperture Telescope for the National Radio Astronomy Observatory*, JPL D-7477 (internal document), Jet Propulsion Laboratory, Pasadena, California, September 1990.

In this article, a recently developed antenna model [4] has been used to analyze wind disturbances. The structural finite-element model, as a part of the antenna model, includes modes of up to 10 Hz. The dynamic wind pressure consists of the spatial pressure on the antenna structure and the wind-force time history. In the new approach presented in this article, the wind force is modeled as a pressure on the antenna dish rather than as an equivalent elevation torque commonly used as a replacement for wind action. Wind-pressure distribution is obtained from the JPL/IDEAS finite-element code,[3] based on wind tunnel measurements [5].[4,5] The wind-force time history is another new addition. It is a linear filter that shapes the wind-force time profile obtained from the Davenport wind-velocity spectrum [6].

The results obtained consist of estimates of pointing error due to static wind pressure and wind gusts for 60- and 90-deg antenna-elevation angles. Results show that the pointing error due to wind turbulence is of the same order as the error due to static pressure, thus it must not be neglected.

II. Wind-Velocity and Wind-Force Models

The wind velocity v is a combination of a steady-state flow (mean velocity, or a quasi-steady component, see [10]) v_m, and a turbulence (gust) v_t

$$v = v_m + v_t \tag{1}$$

The component v_t is a random process with zero mean and standard deviation σ_v. The standard deviation and other wind parameters are determined from the Davenport model [5,7]. In this model, the wind-velocity spectrum S_v for the wind at a height of 10 m is as follows:

$$S_v(f) = 4v_S^2 f^{-1}\frac{x^2}{(1+x^2)^{4/3}} \tag{2}$$

[3] R. Levy and D. Strain, JPL-IDEAS Finite Element Analysis and Design Optimization Program, JPL NPO-17783 (internal document), Jet Propulsion Laboratory, Pasadena, California, October 1988.

[4] R. B. Blaylock, "Aerodynamic Coefficients for a Model of a Paraboloidal Reflector Directional Antenna Proposed for a JPL Advanced Antenna System," JPL Memorandum CP-6 (internal document), Jet Propulsion Laboratory, Pasadena, California, May 1, 1964.

[5] N. L. Fox, "Load Distributions on the Surface of Paraboloidal Reflector Antennas," JPL Memorandum CP-4 (internal document), Jet Propulsion Laboratory, Pasadena, California, July 1962.

where f is the frequency in hertz; v_s is the shear velocity of the flow in meters per second, see [7]; x is the dimensionless frequency, $x = 1,200f/v_m$; and v_m in meters per second is the mean velocity at 10 m. Denoting $\kappa = (v_s/v_m)^2$ as the surface drag coefficient [Eq. (2)] gives

$$S_v(f) = 4,800v_m\left(\frac{\kappa x}{(1+x^2)^{4/3}}\right) \tag{3}$$

The surface drag coefficient is obtained from the roughness of the terrain, see [7]

$$\kappa = \left(2.5ln(z/z_o)\right)^{-2} \tag{4}$$

where z is the distance from the ground (z = 10 m) and z_o is the roughness length (5–20 cm in the DSS-13 environment). For the roughness z_o = 0.05 m, one obtains $\kappa = 0.0057$; and for $z_o = 0.2$ m, $\kappa = 0.0105$, which agrees with estimates by Levy and McGinness [7] of κ at the antenna site in Goldstone, California.

It is well known (see [8]) that the standard deviation of a stationary process can be determined from its spectrum, namely

$$\sigma_v = \left(T_v(\infty) - T_v(0)\right)^{1/2} \tag{5a}$$

where

$$T_v(f) = \int_0^f S_v(v)dv = 6\kappa v_m^2\left(1-(1+x)^{-1/3}\right) \tag{5b}$$

thus,

$$\sigma_v = \alpha v_m, \qquad \alpha = (6\kappa)^{1/2} \tag{6}$$

For a typical surface drag coefficient κ = 0.005–0.010, one obtains α = 0.17–0.25.

Although the force acts on the whole antenna structure, in this article the wind force is assumed to act only on the antenna dish. This is a fair assumption, since most of the wind energy is absorbed by the tipping structure. The force distribution on the dish surface yields important information for determining the wind action on the antenna. By using the available quasi-static wind-tunnel data,[6,7] the spatial force distribution can be obtained from the JPL-IDEAS model.[8] As a result, the wind force as a time and spatial variable becomes a time variable in the dynamic model. In the antenna model, the force acting on the dish has two components: F_x and F_y (wind from x and y directions). Since the time characteristics of the wind force do not depend on its direction, it is not necessary to distinguish the direction, thus the wind force is simply denoted by F.

Statistical properties of the wind force are determined from the previously described wind-velocity parameters. At a given height, the force is proportional to the square of the velocity [9]

$$F = kv^2 \tag{7}$$

and the velocity consists of a constant mean flow with a superimposed fluctuation, as in Eq. (1). Therefore, the force is decomposed into a steady force F_m and a turbulent force F_t with zero mean value

$$F = F_m + F_t \tag{8}$$

The static force F_m (lb) is determined for the speed v_m (mph)

$$F_m = F(v_m) = kv_m^2 = \alpha_w^2 F_{om} \tag{9}$$

where $\alpha_w = v_m/100, F_{om} = 1$ lb is the force at a wind velocity of 100 mph, and $k = 0.0001F_{om}$. The gust F_t, on the other hand, is determined as follows:

$$F_t = \alpha_f v_t \tag{10}$$

where $\alpha_f = \partial F/\partial v\,|_{v=v_m} = 2kv_m = 2F_m/v_m$ depends on the wind velocity v_m. From Eq. (10) the wind-force spectrum can be obtained as follows:

$$S_f(f) = \alpha_f^2 S_v(f) \tag{11}$$

Thus, the standard deviation σ_f of the gust is

$$\sigma_f = |\alpha_f|\sigma_v \tag{12}$$

[6] R. B. Blaylock, op. cit.

[7] N. L. Fox, op. cit.

[8] R. Levy and D. Strain, op. cit

Finally, by introducing Eq. (6) to Eq. (12), one obtains

$$\sigma_f = 2\alpha F_m \tag{13}$$

for the static force F_m given by Eq. (9).

III. Wind-Force Simulations

Static and dynamic wind forces have been simulated. The static force is determined from Eq. (9), and the static force simulations are obvious. The dynamic force is generated by a filter with a transfer function $T(f)$

$$T(f) = \frac{a_o + a_1 s + a_2 s^2 + \ldots + a_m s^m}{b_o + b_1 s + b_2 s^2 + \ldots + b_m s^m} \tag{14}$$

The parameters a_1 and b_1, $i = 1, \ldots, m$, $m > 0$ are determined so that the power spectrum of $T(f)$ is the best approximation of the wind-power spectrum $S_f(f)$. For this purpose, the square root s_f of the power spectrum S_f is used

$$s_f(f) = \left(S_f(f)\right)^{1/2} \tag{15}$$

The order m of the filter and the parameters a_1 and $b_i, i = 1, \ldots, m$ can be determined. For the frequency interval $[f_1, f_2]$, $f_2 > f_1$, denote the norm $\|\,.\,\|_w$ of a function $g(f)$ as

$$\| g \|_w = \left(\int_{f1}^{f2} w(f) g^2(f) df\right)^{1/2} \tag{16}$$

where $w(f) > 0$, $f \epsilon [f_1, f_2]$ is a weighting function. Denote the poles of the transfer function $\lambda_i, i = 1, \ldots, m$, then the filter parameters, and the filter order should be found so that the index J, defined as follows,

$$J = \| s_f(f) - |T(f)| \|_w \tag{17}$$

is minimal, subject to constraints

$$Re(\lambda_i) < 0, \qquad \text{for } i = 1, \ldots, m \tag{18}$$

The constraints assure filter stability.

The plot of the function $s_f(f)$, obtained from Eq. (15) (the Davenport model for 30-mph wind speed), is shown by the solid line in Fig. 1. A linear filter that generates the wind force of a spectrum close to the Davenport model is determined by minimizing J subject to constraints in Eq. (18). The values of the Davenport spectrum for high frequencies (in the case considered for frequencies 1–1,000 Hz) are small; therefore, they should be weighted significantly to obtain a good fit in this frequency range. The following weights have been assigned: $w = 3$ for frequencies 0.1–1 Hz, $w = 10$ for 1–10 Hz, $w = 30$ for 10–100 Hz, and $w = 100$ for 100–1,000 Hz. For different integers m, the index J has been minimized; the integer $m = 4$ was found to be the lowest filter order for which the results have been satisfactory. The filter parameters for the minimal solution are:

$$a_0 = 0.00037,\ a_1 = -0.92431, a_2 = -138.7468,$$
$$a_3 = -56.4776,\ a_4 = -0.03952$$
$$b_0 = -0.000306,\ b_1 = -0.18103,\ b_2 = -8.7769,$$
$$b_3 = -57.9502,\ b_4 = -11.8569$$

The magnitude of the filter-transfer function is shown by the dashed line in Fig. 1. The figure shows a good approximation of the Davenport spectrum within the interval of interest $[f_1 = 0.001, f_2 = 10]$ Hz. The wind force generated by the filter for 30-mph wind is shown in Fig. 2.

A similar approach was used to determine wind filters and wind forces for wind velocities $v_m = 10$, 20, 40, and 50 mph.

IV. Pointing-Error Simulations

The antenna state-space model with the position loop closed, described in [4], is as follows:

$$\dot{x} = Ax + B_c u + B_w F, \qquad y = Cx + Du \tag{19}$$

where x is a state vector $n \times 1; u$ is the command signal $p \times 1; F$ is the wind force (single input); y is the output $q \times 1$. The input matrix B_w is determined so that for a wind of 100 mph, a static wind force $F_{om} = 1$ lb is applied. The plot of drag force versus antenna-elevation angle obtained from the wind-tunnel experiment[9] is shown in Fig. 3. In this article, two elevation positions of the antenna are simulated: 90 deg and 120 deg (that is, 60 deg with wind blowing from behind the dish). Note from Fig. 3 that the drag is almost the same for the both positions. Nevertheless, it will be shown later that the effects of the wind actions on the antenna are distinct.

Since the antenna model is linear, the static force (mean wind force) and dynamic force (gust force) are simulated separately. However, they can be superimposed, if necessary. For the static wind disturbances the system with the position loop closed [represented by Eq. (19)] is simulated with the zero command signal u and constant wind disturbance F_m. The steady-state response (elevation and cross-elevation pointing error) is obtained for a 60- and 90-deg antenna-elevation angle. The plots of pointing error due to static wind from the x and y directions for different wind speeds are shown in Fig. 4. The following results for static wind load are obtained: For 30-mph x-direction wind, the elevation pointing error is 9.0 mdeg for a 60-deg elevation angle and 1.7 mdeg for a 90-deg elevation angle. The cross-elevation pointing error is 5.8 mdeg for a 60-deg elevation angle and 6.6 mdeg for a 90-deg elevation angle. For 30-mph y-direction wind, the elevation pointing error is 1.1 mdeg for a 60-deg elevation angle and 1.3 mdeg for a 90-deg elevation angle; the cross-elevation pointing error is 0.13 mdeg for a 60-deg elevation angle and 0.22 mdeg for a 90-deg elevation angle. The small pointing error due to wind in the y direction is a result of the integrating action of the controller.

The gust wind load was applied to the antenna model. The responses of the antenna (elevation and cross-elevation pointing errors, elevation and azimuth encoder readings) are presented in Fig. 5 for x-direction wind and in Fig. 6 for y-direction wind. Wind force was simulated for velocities 10, 20, 30, 40, and 50 mph for 60- and 90-deg elevation angles of the antenna. The results are presented in Fig. 7 for x-direction wind and 60-deg elevation angle (solid line) and 90-deg elevation angle (dashed line). Figure 8 shows the results for y-direction wind. Note that like the results of the static load, the results of the dynamic loading show the pointing errors to be proportional to the square of the velocity (the symbols "o" in Figs. 7 and 8 denote the simulation results, and the lines denote the least-squares quadratic approximation). It can be seen in Fig. 8 that the integrating action of the controller annihilated a significant part of the pointing error due to static y-direction wind; however, the dynamic part of the y-direction wind is not compensated for by the controller, which causes a significant pointing error.

The spectra of the wind-gust response were analyzed. The spectra of the elevation and cross-elevation pointing

[9] Engineering Data 34-M Antenna, JPL Drawing 9493280 (internal document), Jet Propulsion Laboratory, Pasadena, California, 1988.

errors, and elevation and azimuth encoder readings for x-direction wind gusts are shown in Fig. 9, and in Fig. 10 for y-direction wind gusts. The spectra show that modes of low frequency (2 Hz), medium (4 Hz), and high frequency (9 Hz) are important in wind-gust simulations.

Finally, a power spectral-density analysis of the pointing errors was performed for the antenna at the 90-deg elevation position, and results were compared with the simulation results of Figs. 5, 6, 9, and 10. The spectral analysis provides a precise measure of root-mean-square (rms) error, limited only by step-size effects. It serves as a convenient method for statistical verification of simulations.

The power spectral-density function of the pointing error $S_\epsilon(f)$ was calculated according to

$$S_\epsilon(f) = W^2(f)\, S_f(f) \tag{20}$$

where $W(f)$ is the amplitude-versus-frequency response function between the respective wind-disturbance inputs and pointing-error outputs of the system described by Eq. (19), and $S_f(f)$ represents the wind-force spectrum from Eq. (11). The corresponding spectral distributions and rms errors were determined from a numerical integration of $S_\epsilon(f)$ over frequency. An integration routine that adopted step size in the vicinity of peaks of $S_\epsilon(f)$ was employed to minimize computational errors.

The frequency-response functions for elevation- and cross-elevation pointing errors are plotted in Figs. 11(a) and (b) for x-axis, and in Figs. 12(a) and (b) for y-axis wind direction. The corresponding power spectral density and spectral distribution functions for pointing errors are shown in Fig. 13 for x-axis winds and in Fig. 14 for y-axis winds. The mean wind velocity in both cases was 30 mph. The rms pointing errors were calculated from the corresponding spectral distribution functions at a frequency of 10.0 Hz. For x-axis direction wind the elevation pointing error is 1.60 mdeg and the cross-elevation pointing error is 5.15 mdeg, while for y-axis direction wind, the elevation pointing error is 5.53 mdeg, and the cross-elevation pointing error is 0.65 mdeg. These errors agree well with the values obtained from simulations of Figs. 5 and 6.

V. Conclusions

Wind forces acting on the antenna structure have been modeled in this article. Their static and dynamic parts have been applied as a disturbance to the closed-loop antenna model at 60- and 90-deg elevation angles. The results show that both the static and dynamic parts of the pointing error are of equal importance, and that despite the dominant presence of low-frequency components in the wind-disturbance spectrum, the high-frequency modes of the antenna have been excited, which caused significant pointing errors. In order to improve the analytical results, experimental verification should be the first priority.

Acknowledgments

The authors thank Roy Levy, Douglas Strain, and Ben Parvin for their extensive and useful discussions.

References

[1] M. S. Katow and H. D. McGinness, *Wind Load Predictions for the 64-Meter-Diameter Antenna*, Technical Report 32-1526, Jet Propulsion Laboratory, Pasadena, California, vol. 15, June 15, 1973.

[2] M. S. Katow, "Aerodynamic Static Differential Pressure Values for the 50 Percent Porous Reflector Dish," *DSN Progress Report 42-29*, vol. July and August 1975, Jet Propulsion Laboratory, Pasadena, California, pp. 60–65, October 15, 1975.

[3] M. Massoudi, "Tracking Error of 100-m Antenna due to Wind Gust," *TDA Progress Report 42-48*, vol. September and October, Jet Propulsion Laboratory, Pasadena, California, pp. 94–101, December 15, 1978.

[4] W. Gawronski and J. A. Mellstrom, "Modeling and Simulations of the DSS 13 Antenna Control System," *TDA Progress Report 42-106*, vol. April–June, Jet Propulsion Laboratory, Pasadena, California, pp. 205–248, August 1991.

[5] R. Levy and D. Kurtz, *Compilation of Wind Tunnel Coefficients for Parabolic Reflectors*, JPL Publication 78-16, Jet Propulsion Laboratory, Pasadena, California, April 15, 1978.

[6] A. G. Davenport, "The Spectrum of Horizontal Gustiness Near the Ground in High Winds," *Journal of Royal Meteorol. Society*, vol. 87, pp. 194–211, 1961.

[7] R. Levy and H. McGinness, *Wind Power Predictions Model*, TM 33-802, Jet Propulsion Laboratory, Pasadena, California, November 1976.

[8] E. Simiu and R. H. Scanlan, *Wind Effects on Structures*, New York: Wiley Interscience, 1978.

[9] J. S. Bendat and A. G. Piersol, *Random Data*, New York: Wiley Interscience, 1986.

[10] J. Vellozzi and E. Cohen, "Gust Response Factors," *Proceedings of the ASCE, Journal of the Structural Division*, vol. 94, no. ST6, pp. 1295–1313, June 1968.

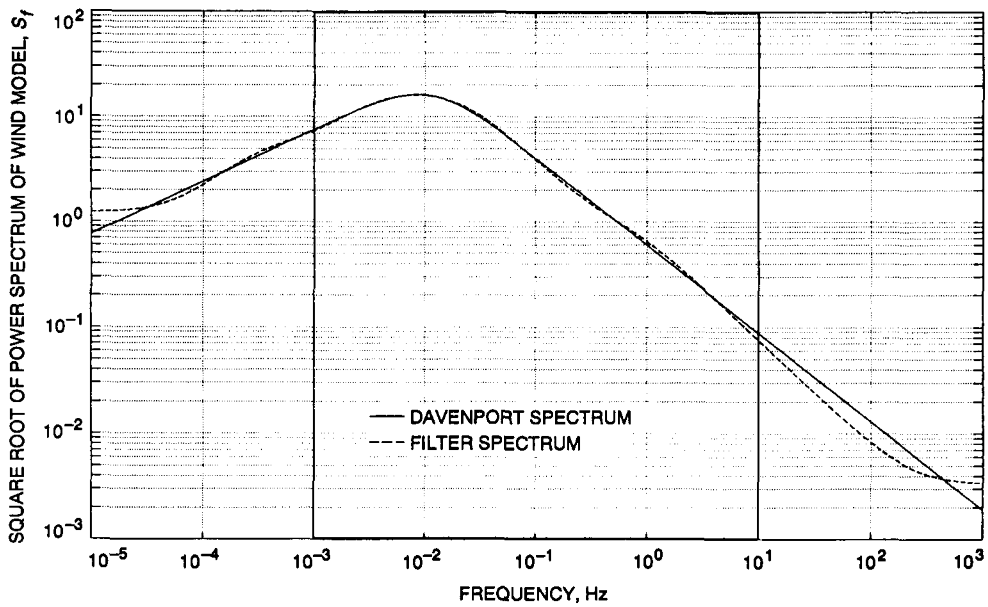

Fig. 1. Square root of power spectrum of the Davenport wind-gust model, for 30-mph wind at the DSS-13 antenna site.

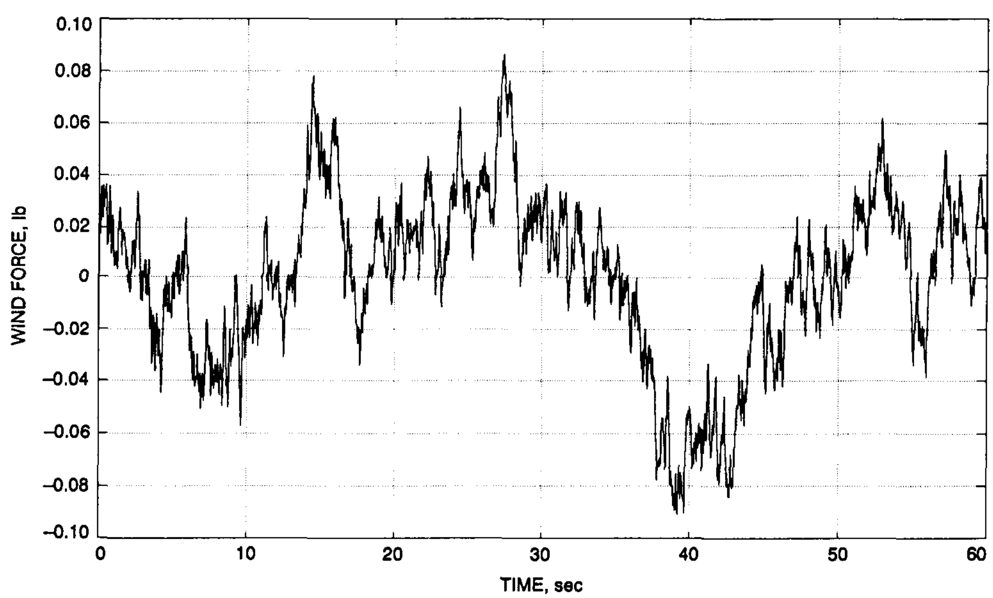

Fig. 2. Wind force generated by the filter for a 30-mph wind gust.

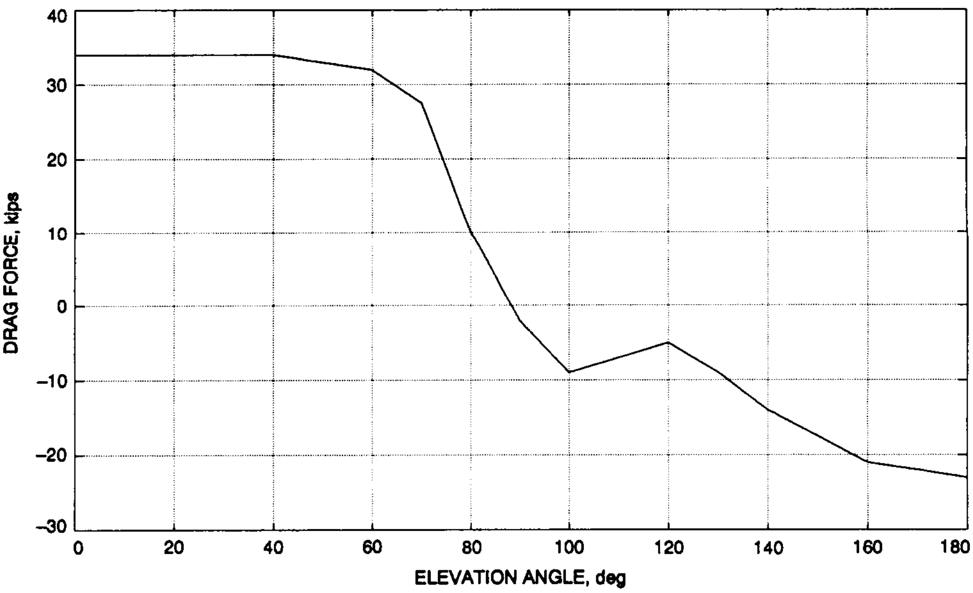

Fig. 3. Experimentally determined wind drag force versus elevation angle.

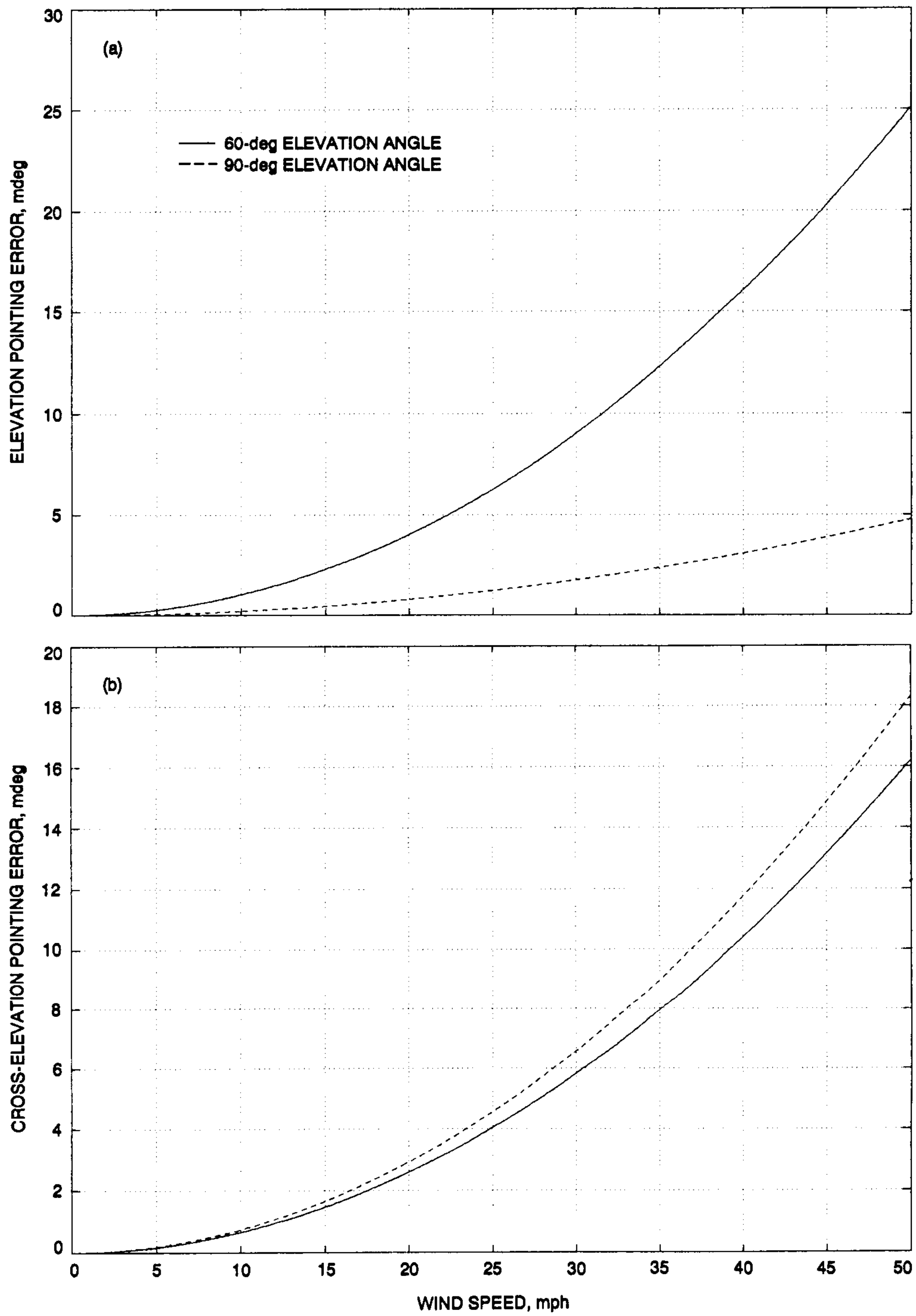

Fig. 4. Pointing error due to static wind from *x*- and *y*-direction for different wind speeds: (a) elevation pointing error; (b) cross-elevation pointing error; (c) elevation encoder reading; and (d) azimuth encoder reading.

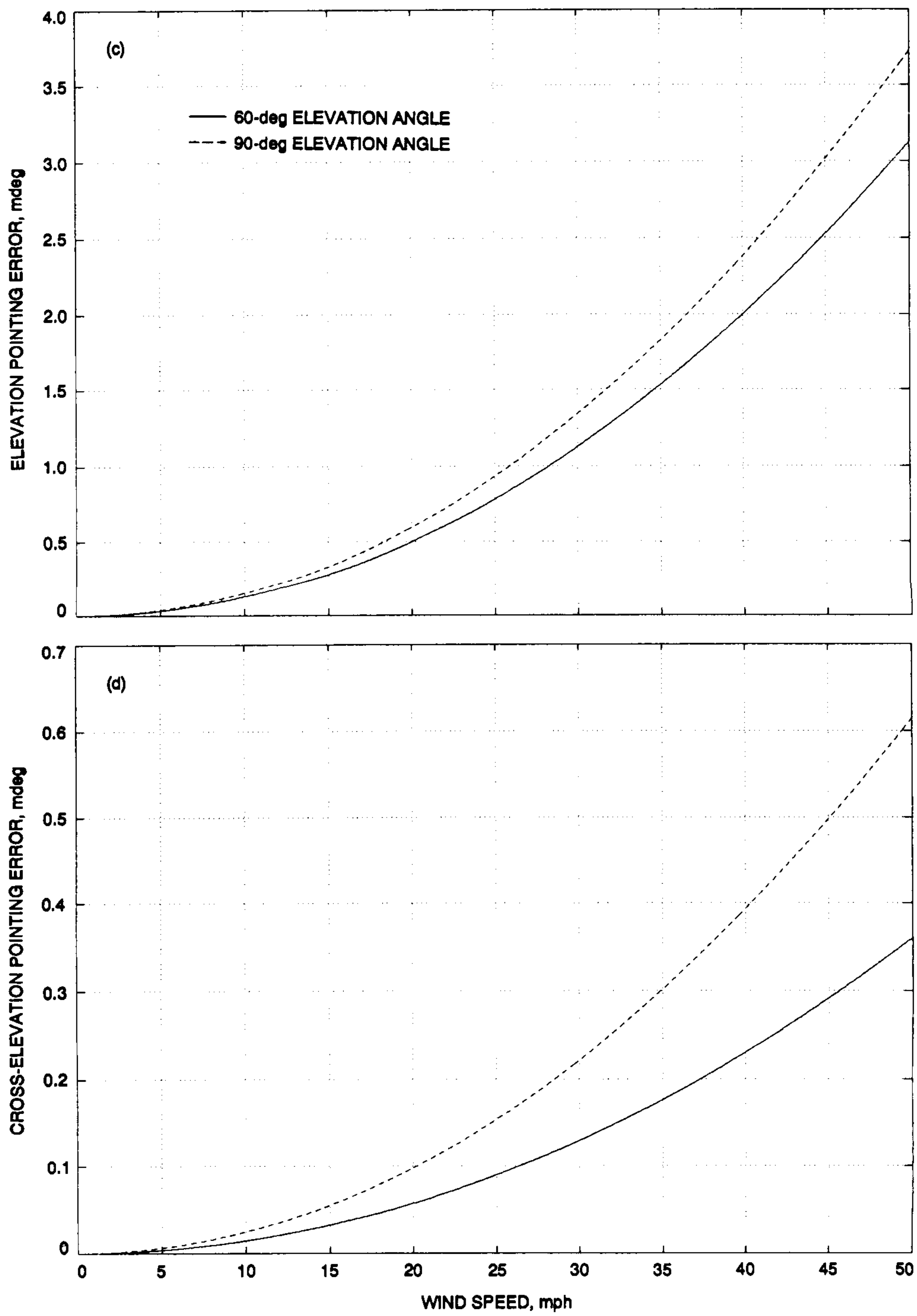

(c)
60-deg ELEVATION ANGLE
90-deg ELEVATION ANGLE
ELEVATION POINTING ERROR, mdeg
4.0
3.5
3.0
2.5
2.0
1.5
1.0
0.5
0
(d)
CROSS-ELEVATION POINTING ERROR, mdeg
0.7
0.6
0.5
0.4
0.3
0.2
0.1
0
0
5
10
15
20
25
30
35
40
45
50
WIND SPEED, mph

Fig. 4 (contd).

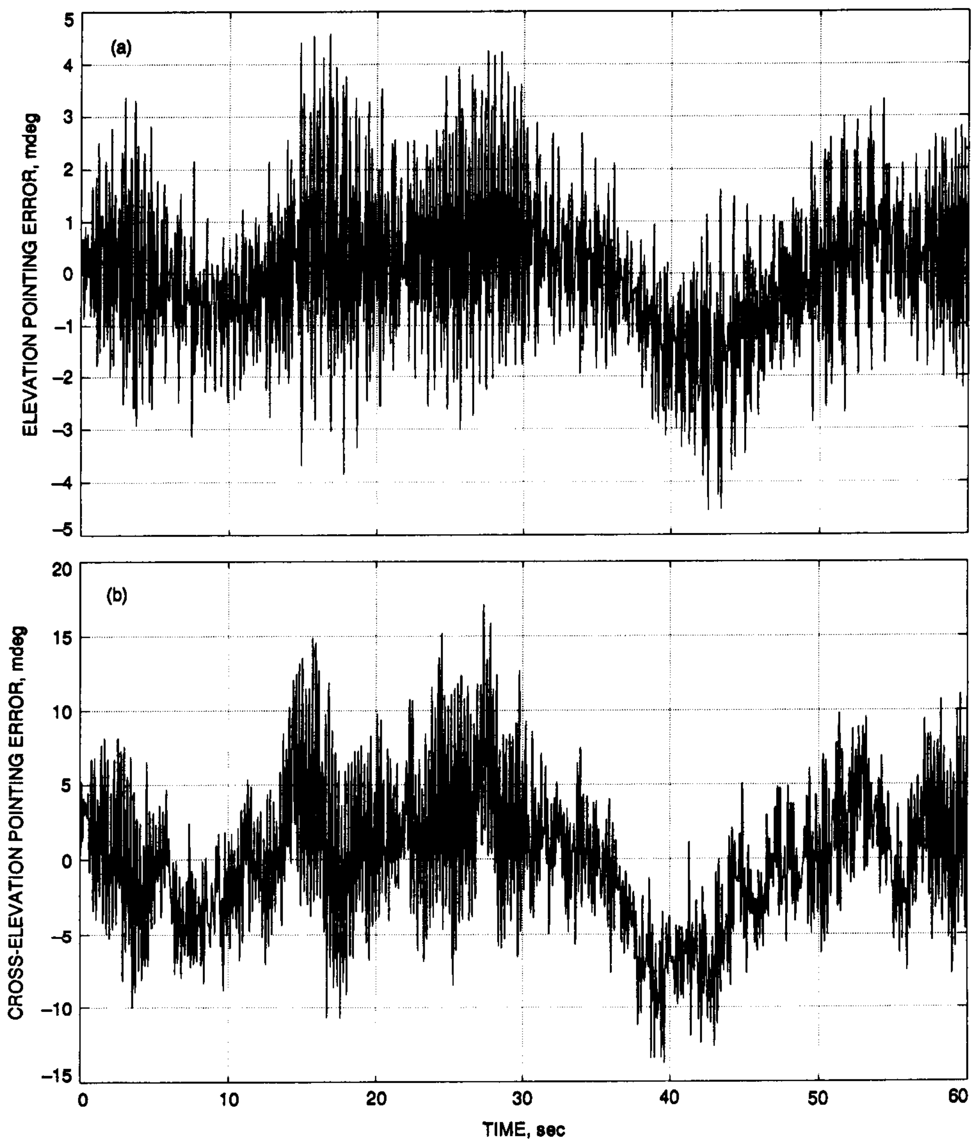

Fig. 5. Antenna responses to x-direction wind: (a) elevation pointing error; (b) cross-elevation pointing error; (c) elevation encoder reading; and (d) azimuth encoder reading.

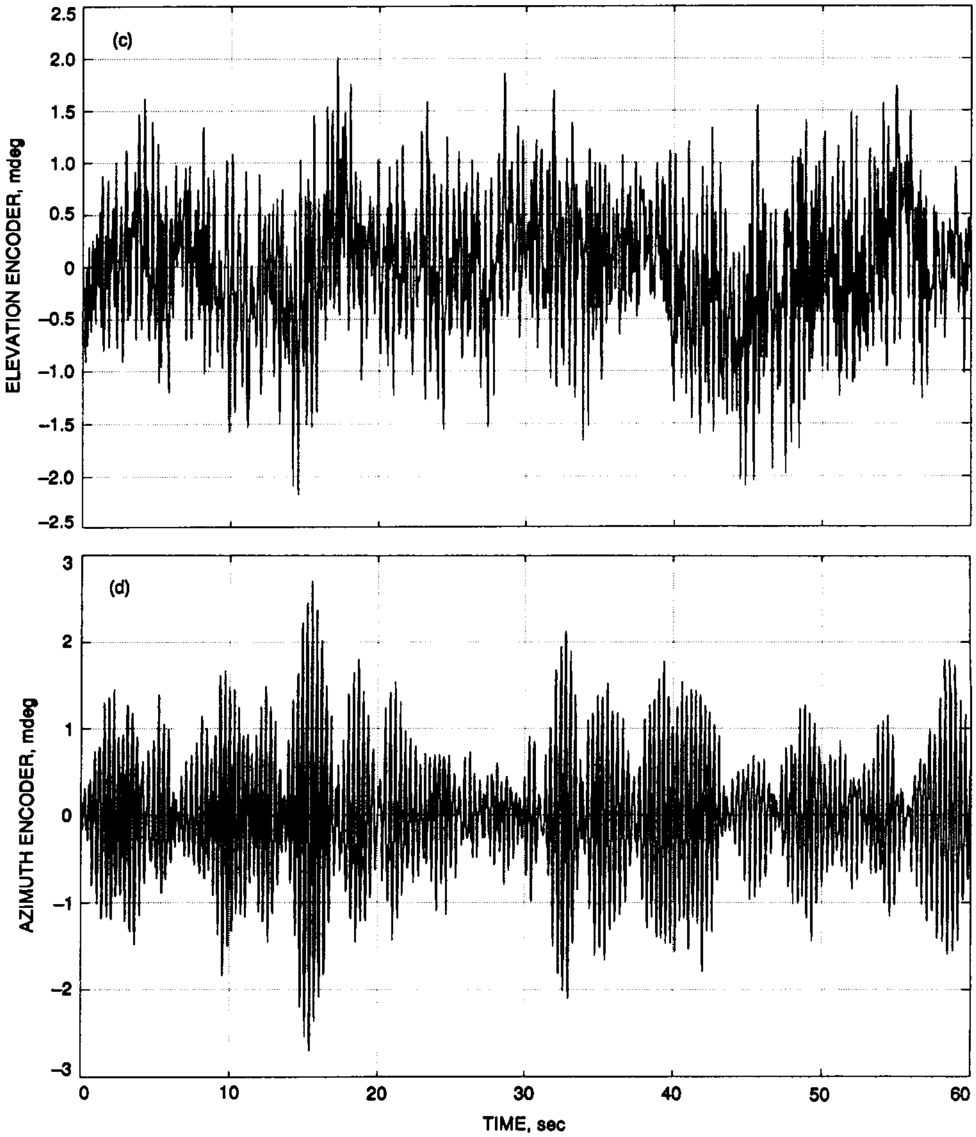

(c)
ELEVATION ENCODER, mdeg
2.5
2.0
1.5
1.0
0.5
0
−0.5
−1.0
−1.5
−2.0
−2.5
(d)
AZIMUTH ENCODER, mdeg
3
2
1
0
−1
−2
−3
0
10
20
30
40
50
60
TIME, sec

Fig. 5 (contd).

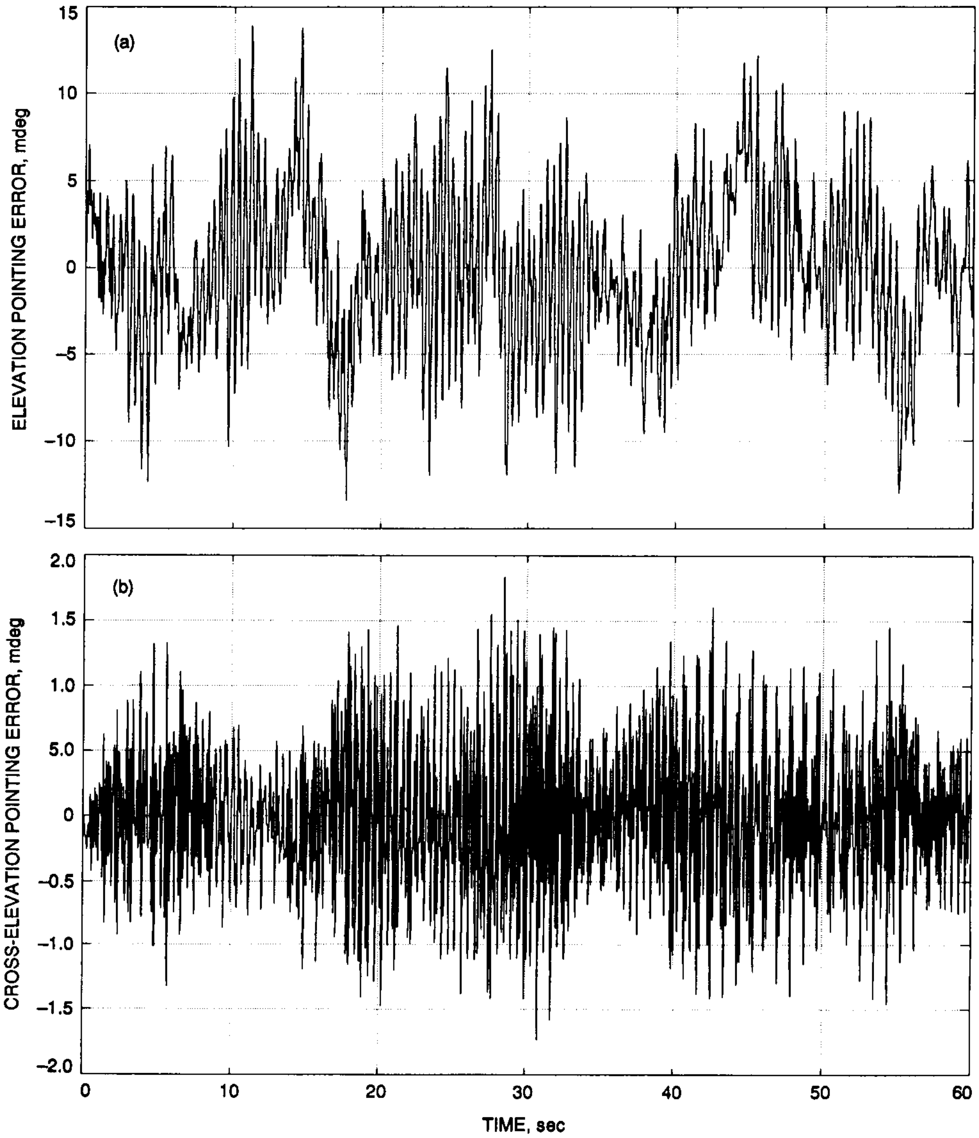

Fig. 6. Antenna responses to *y*-direction wind: (a) elevation pointing error; (b) cross-elevation pointing error; (c) elevation encoder reading; and (d) azimuth encoder reading.

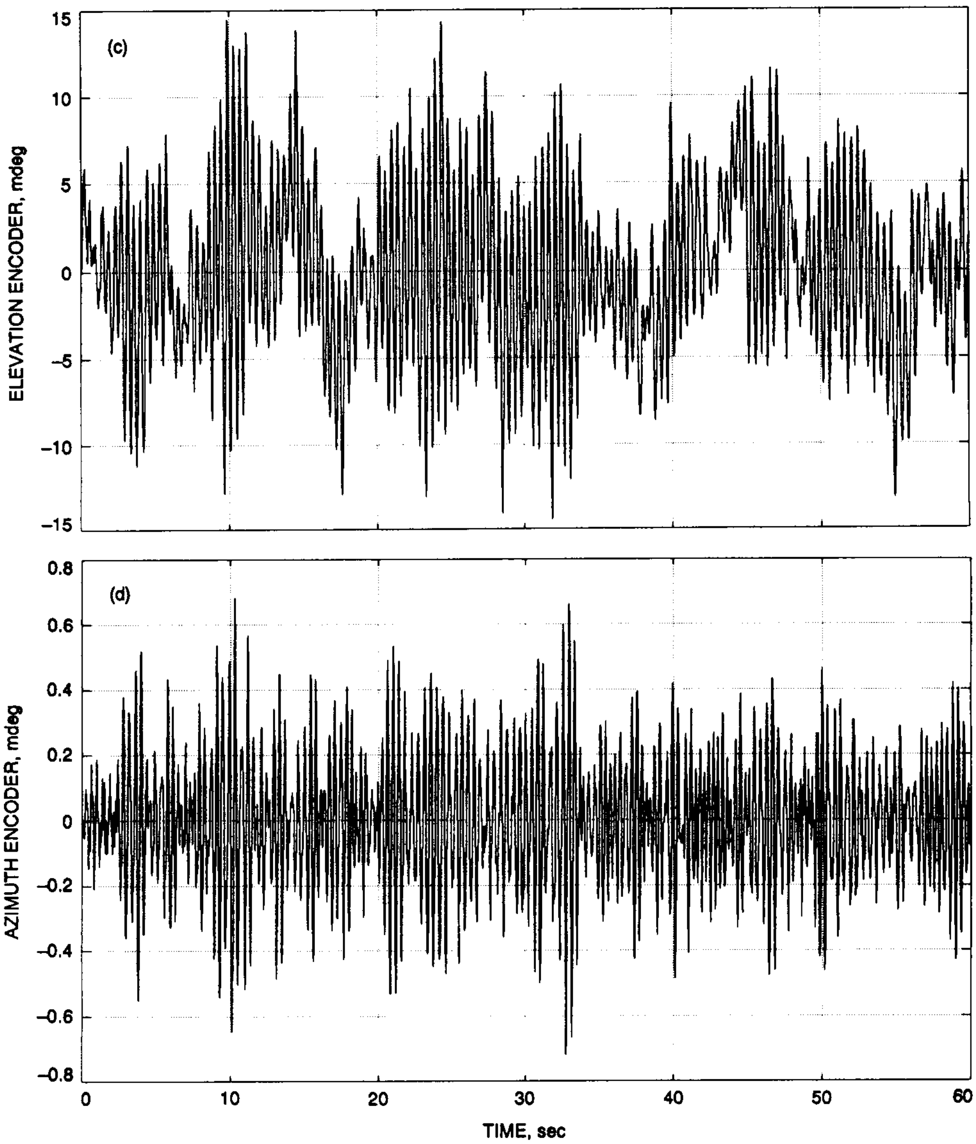
(c)
15
10
5
0
−5
−10
−15
ELEVATION ENCODER, mdeg
(d)
0.8
0.6
0.4
0.2
0
−0.2
−0.4
−0.6
−0.8
AZIMUTH ENCODER, mdeg
0
10
20
30
40
50
60
TIME, sec

Fig. 6 (contd).

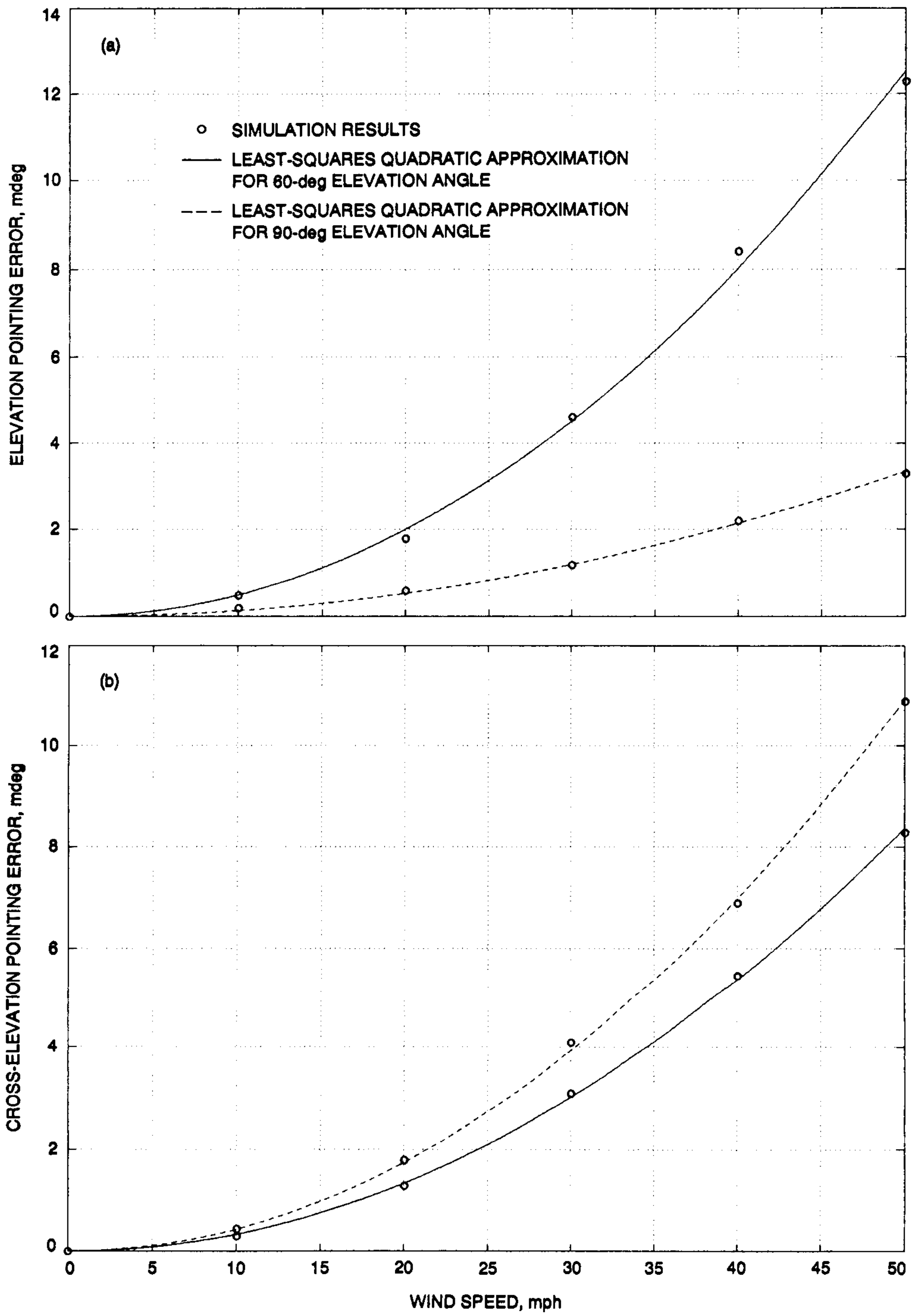

Fig. 7. The quadratic law for x-direction wind gusts: (a) elevation pointing error; (b) cross-elevation pointing error; (c) elevation encoder reading; and (d) azimuth encoder reading.

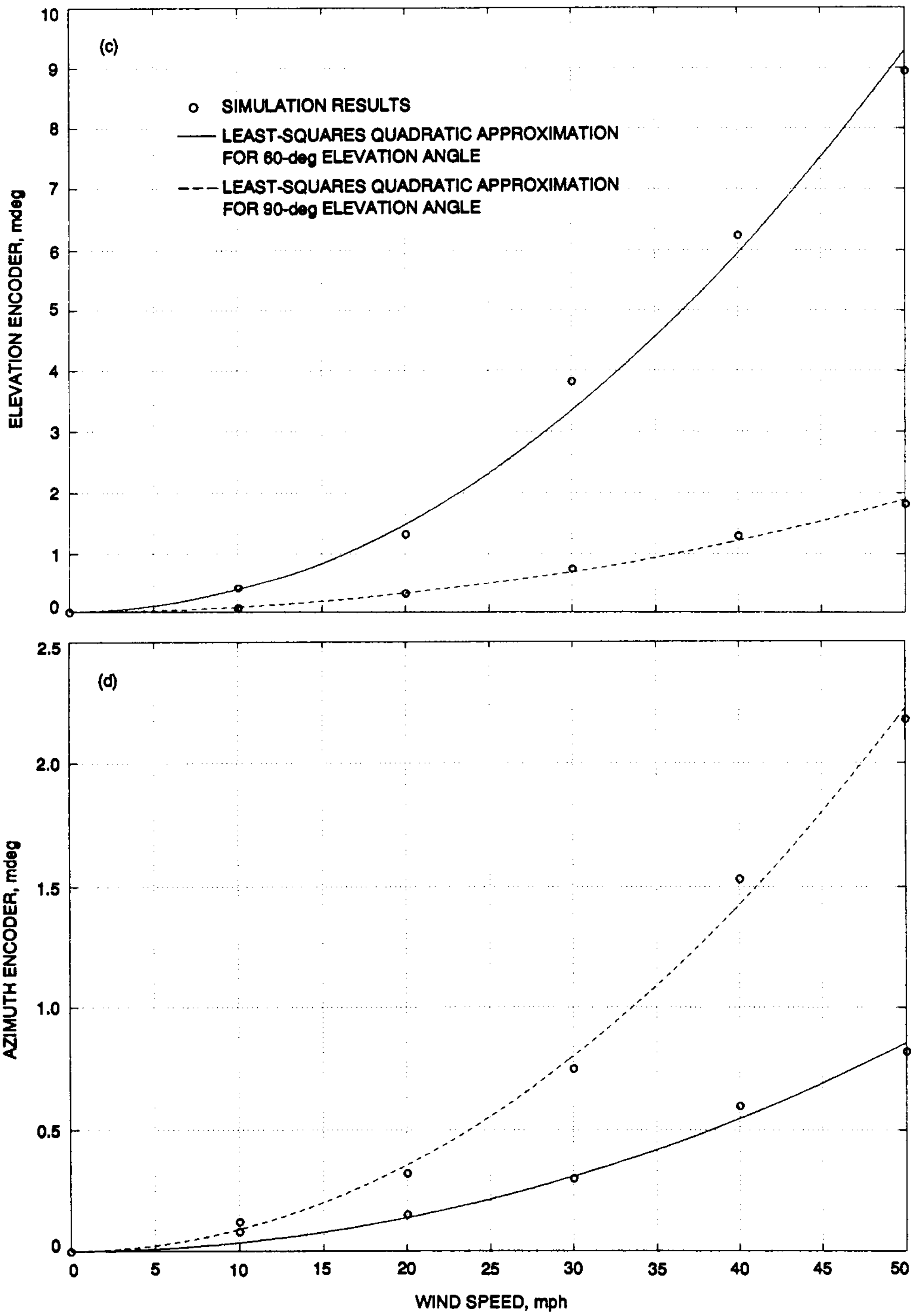

(c)
SIMULATION RESULTS
LEAST-SQUARES QUADRATIC APPROXIMATION FOR 60-deg ELEVATION ANGLE
LEAST-SQUARES QUADRATIC APPROXIMATION FOR 90-deg ELEVATION ANGLE
ELEVATION ENCODER, mdeg
0
1
2
3
4
5
6
7
8
9
10
(d)
AZIMUTH ENCODER, mdeg
0
0.5
1.0
1.5
2.0
2.5
0
5
10
15
20
25
30
35
40
45
50
WIND SPEED, mph

Fig. 7 (contd).

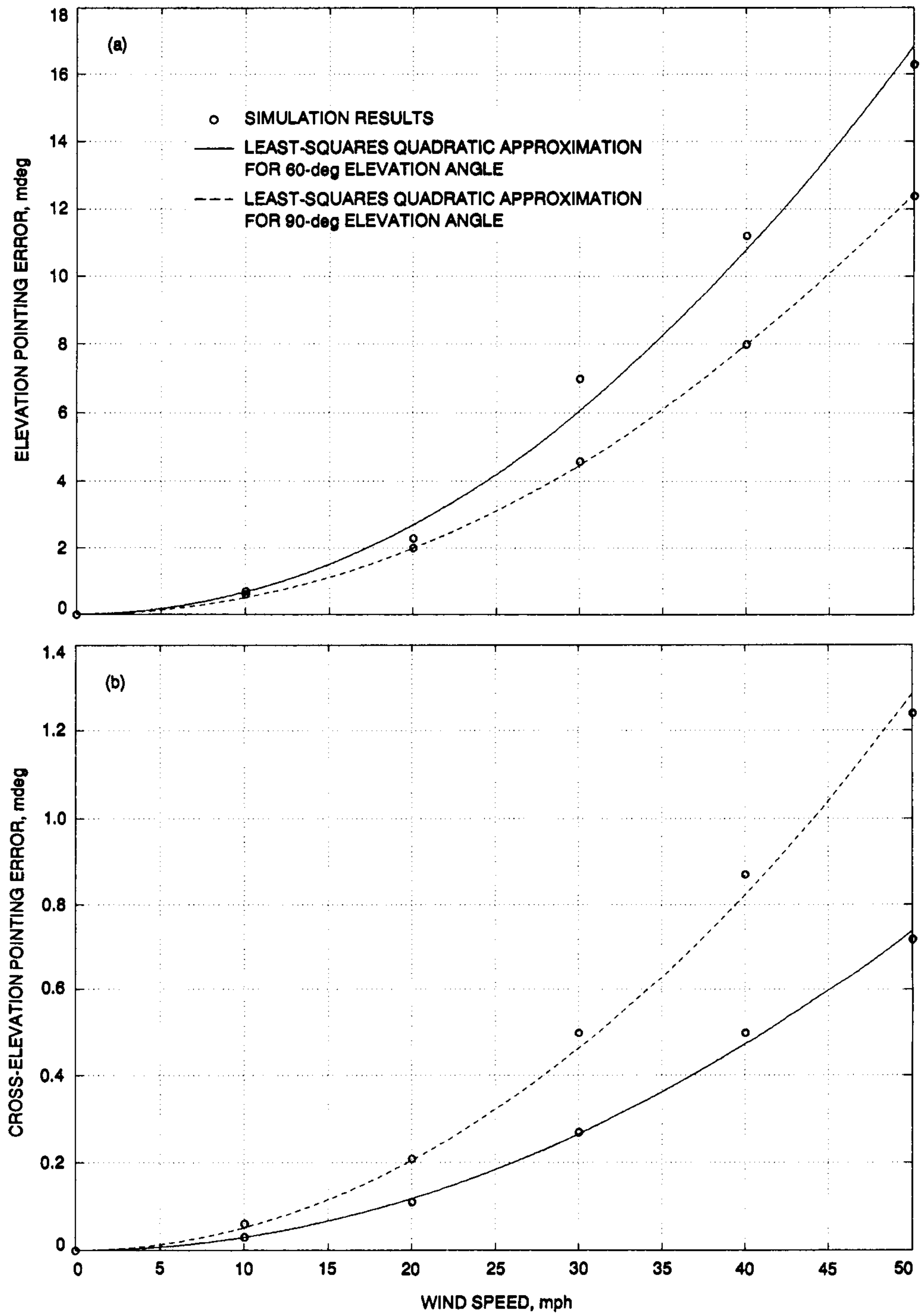

Fig. 8. The quadratic law for y-direction wind gusts: (a) elevation pointing error; (b) cross-elevation pointing error; (c) elevation encoder reading; and (d) azimuth encoder reading.

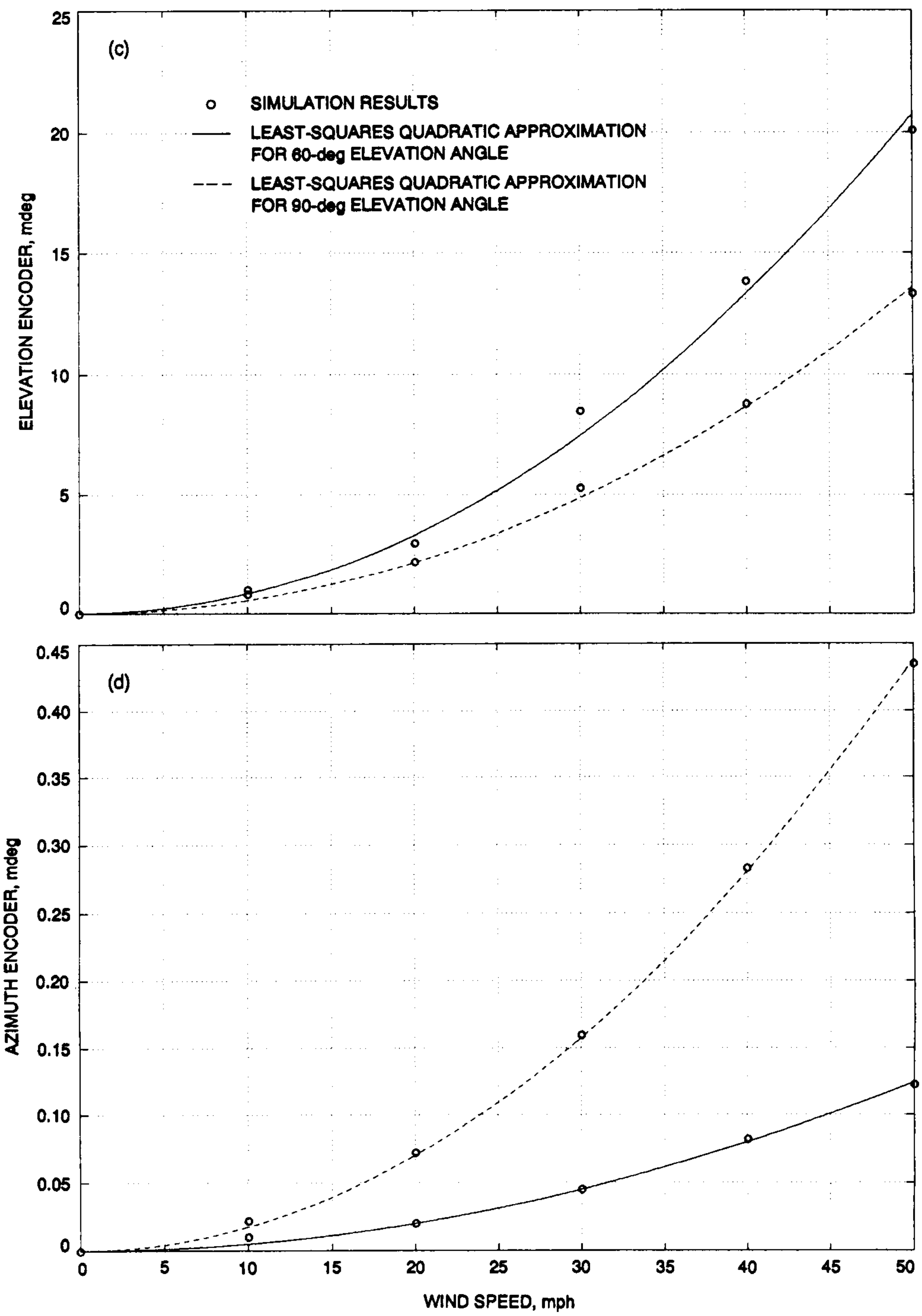
(c)
SIMULATION RESULTS
LEAST-SQUARES QUADRATIC APPROXIMATION FOR 60-deg ELEVATION ANGLE
LEAST-SQUARES QUADRATIC APPROXIMATION FOR 90-deg ELEVATION ANGLE
ELEVATION ENCODER, mdeg
0
5
10
15
20
25
(d)
AZIMUTH ENCODER, mdeg
0
0.05
0.10
0.15
0.20
0.25
0.30
0.35
0.40
0.45
0
5
10
15
20
25
30
35
40
45
50
WIND SPEED, mph

Fig. 8 (contd).

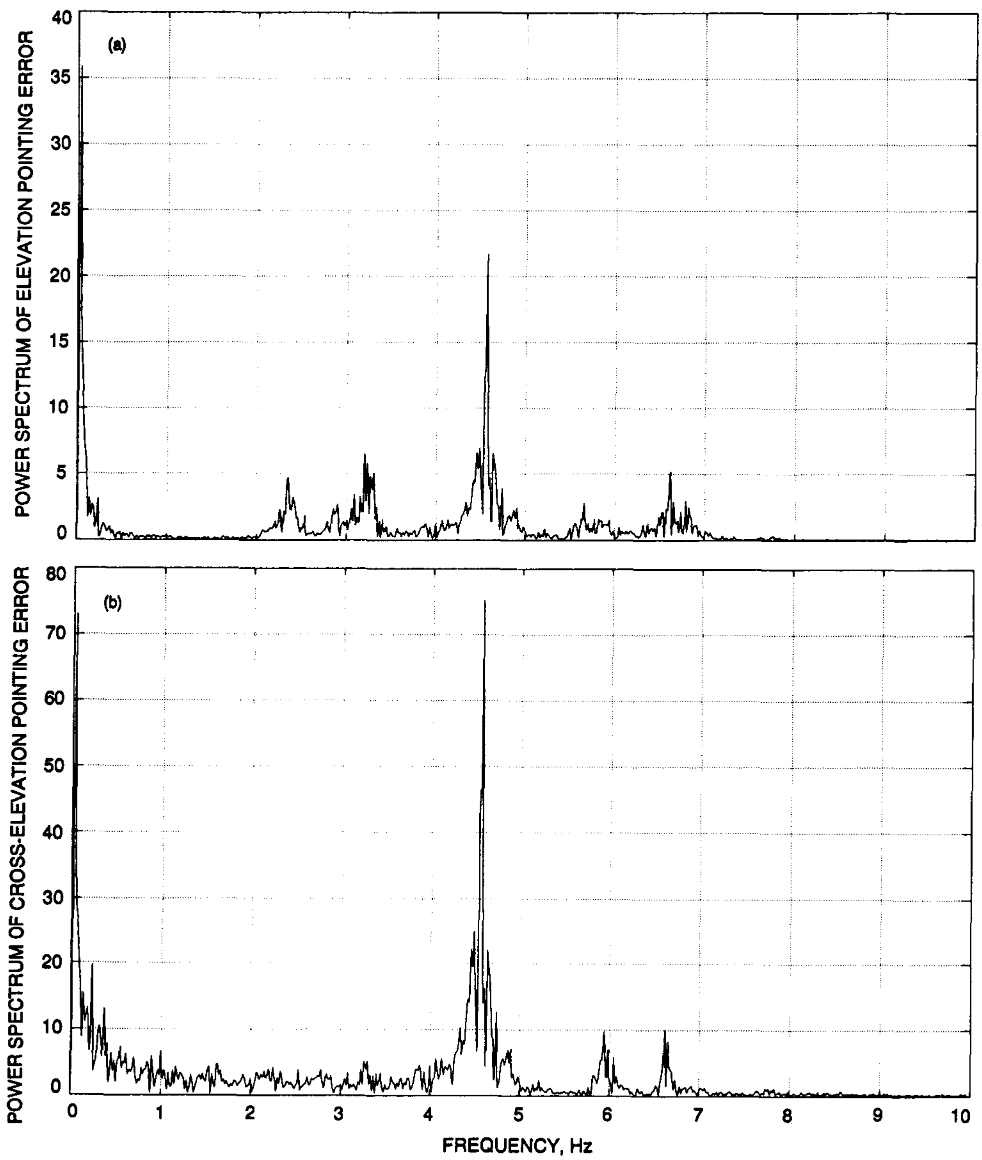

Fig. 9. Spectra for *x*-direction wind gusts: (a) elevation pointing error; (b) cross-elevation pointing error; (c) elevation encoder reading; and (d) azimuth encoder reading.

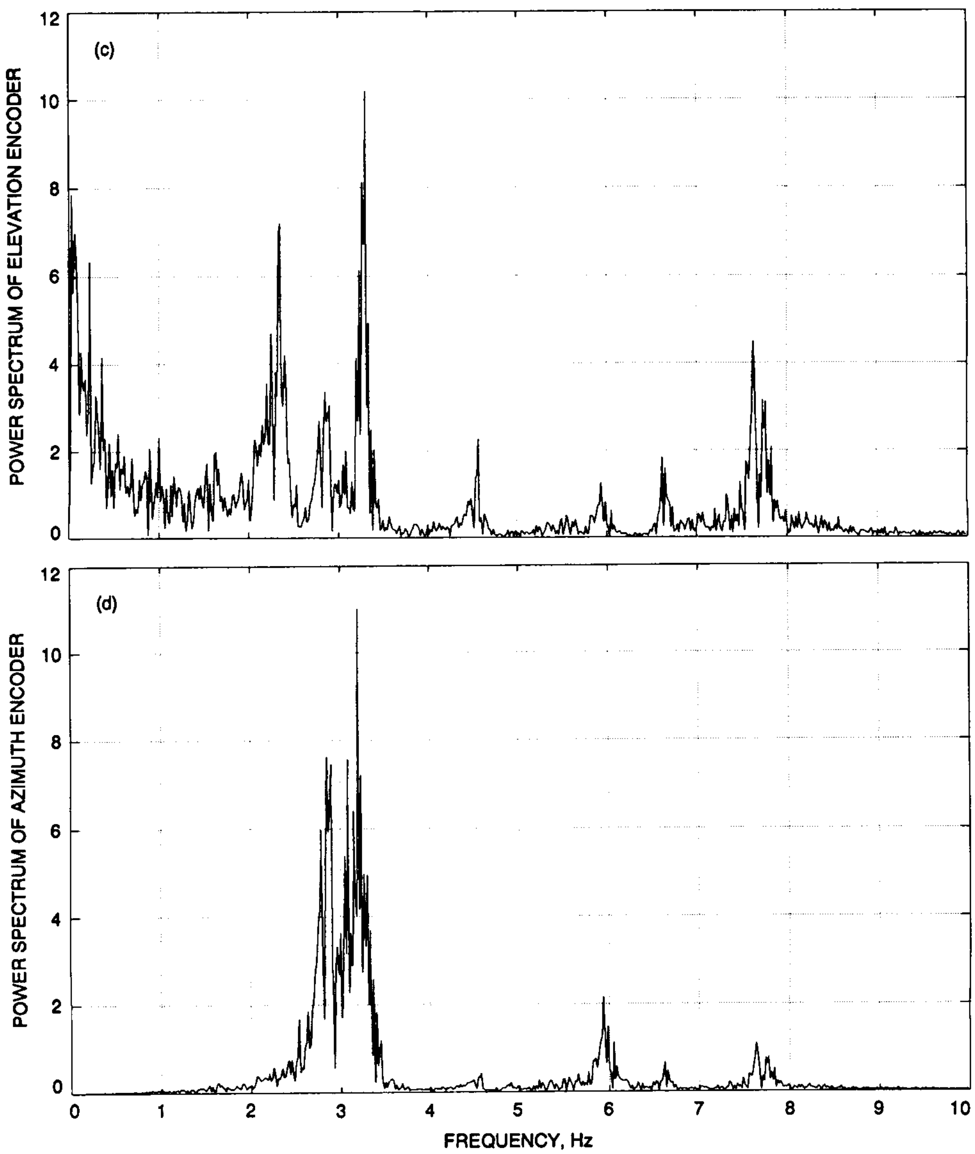
(c)
(d)
POWER SPECTRUM OF ELEVATION ENCODER
POWER SPECTRUM OF AZIMUTH ENCODER
0
2
4
6
8
10
12
FREQUENCY, Hz
0
1
2
3
4
5
6
7
8
9
10

Fig. 9 (contd).

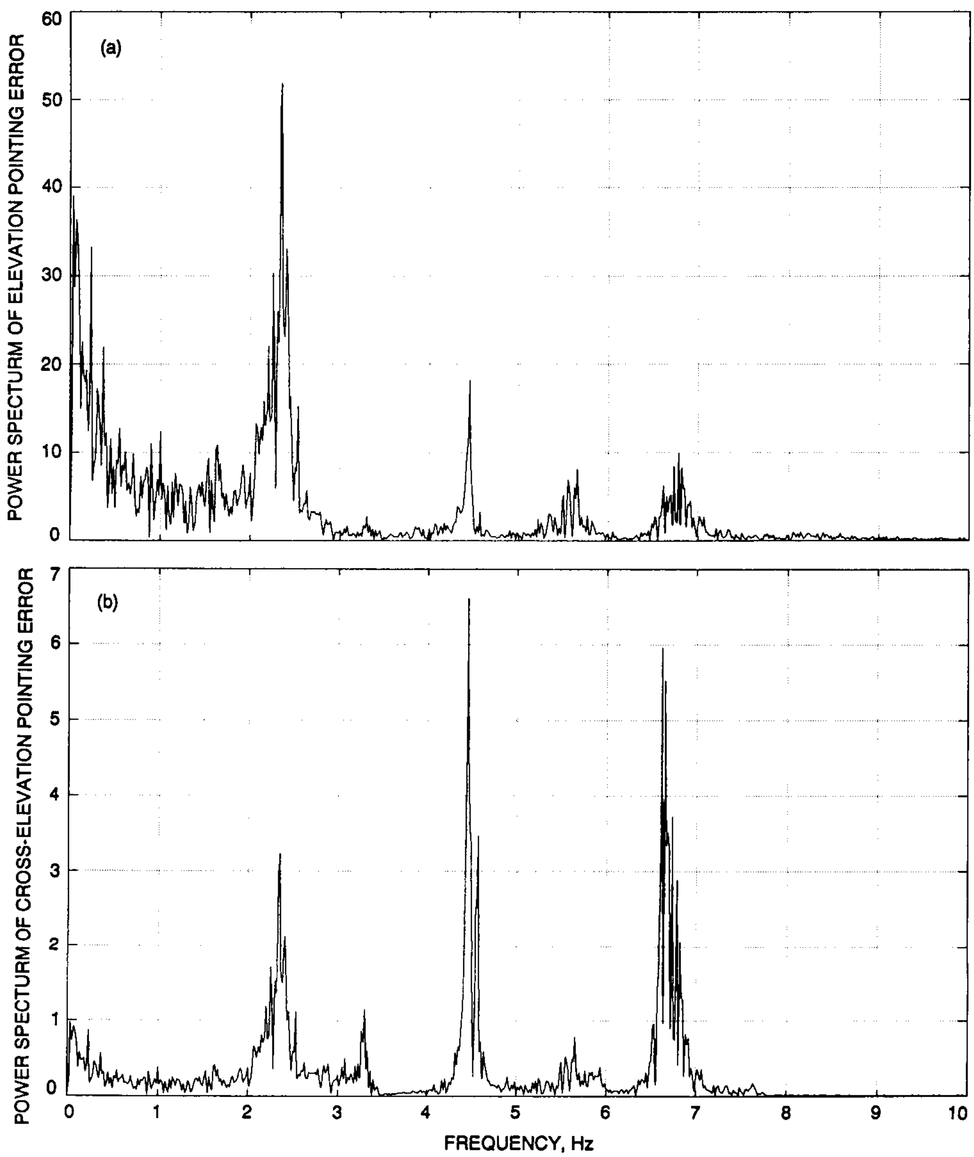

Fig. 10. Spectra for *y*-direction wind gusts: (a) elevation pointing error; (b) cross-elevation pointing error; (c) elevation encoder reading; and (d) azimuth encoder reading.

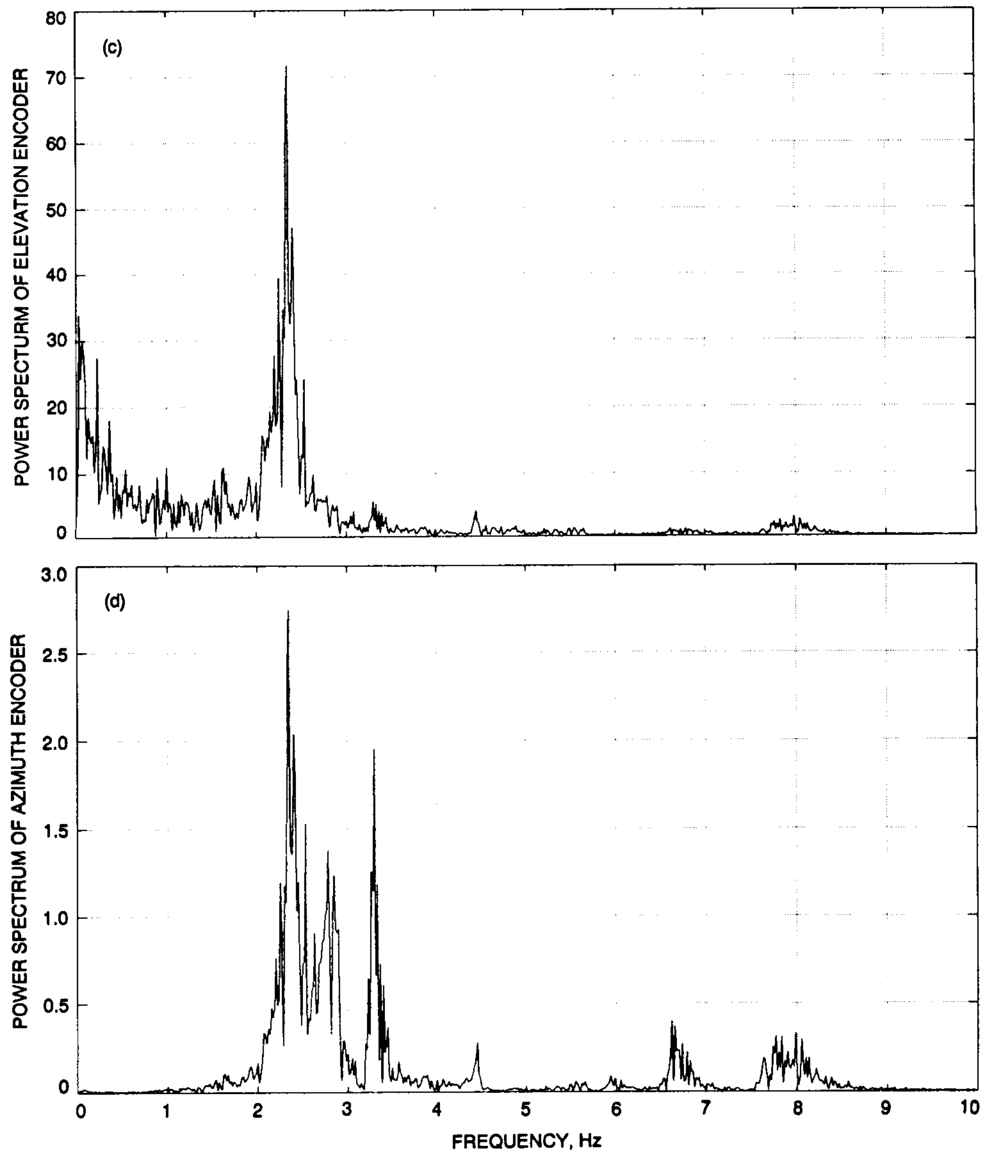
(c)
POWER SPECTURM OF ELEVATION ENCODER
80
70
60
50
40
30
20
10
0
(d)
POWER SPECTRUM OF AZIMUTH ENCODER
3.0
2.5
2.0
1.5
1.0
0.5
0
0
1
2
3
4
5
6
7
8
9
10
FREQUENCY, Hz

Fig. 10 (contd).

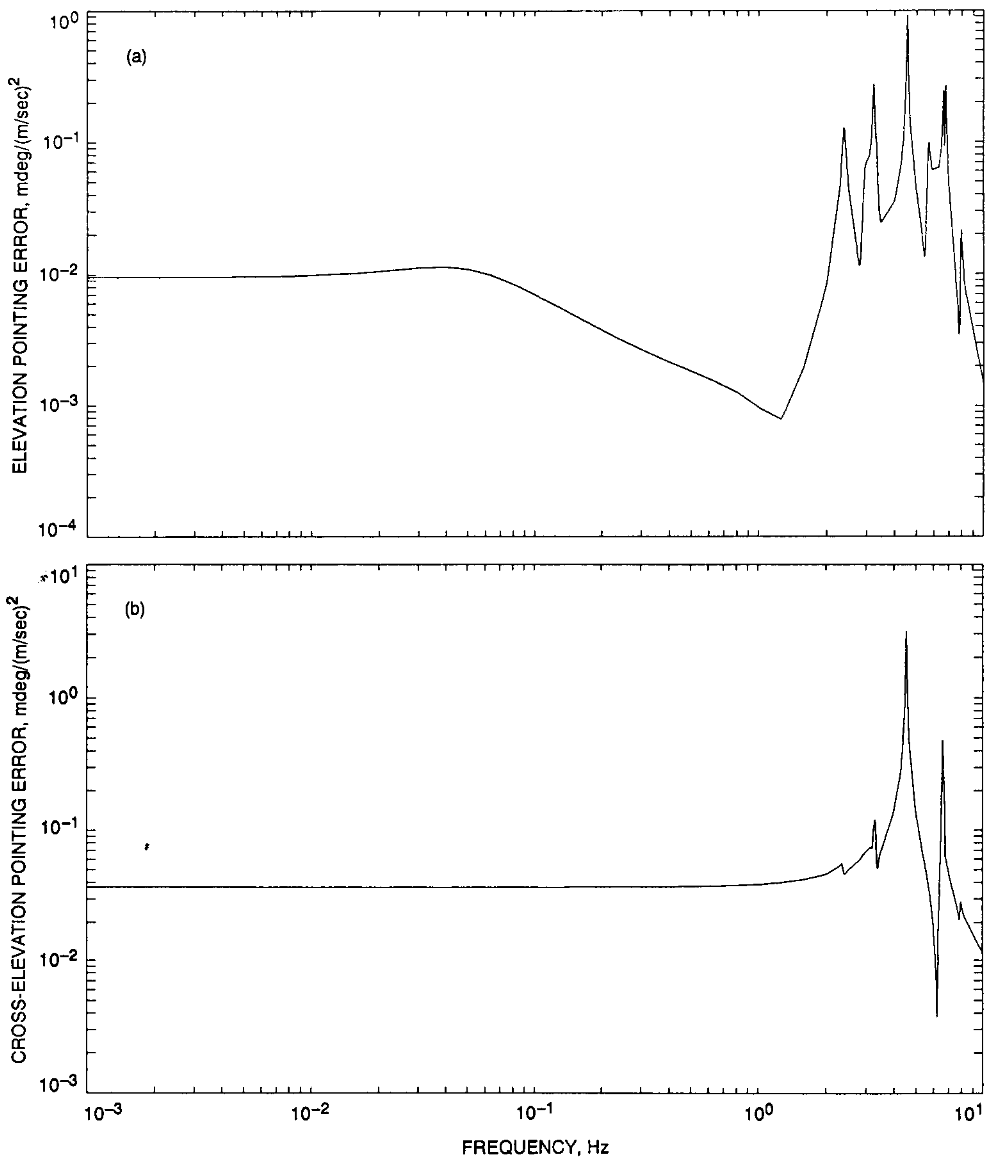

Fig. 11. Frequency-response functions for *x*-direction wind: (a) elevation pointing error and (b) cross-elevation pointing error.

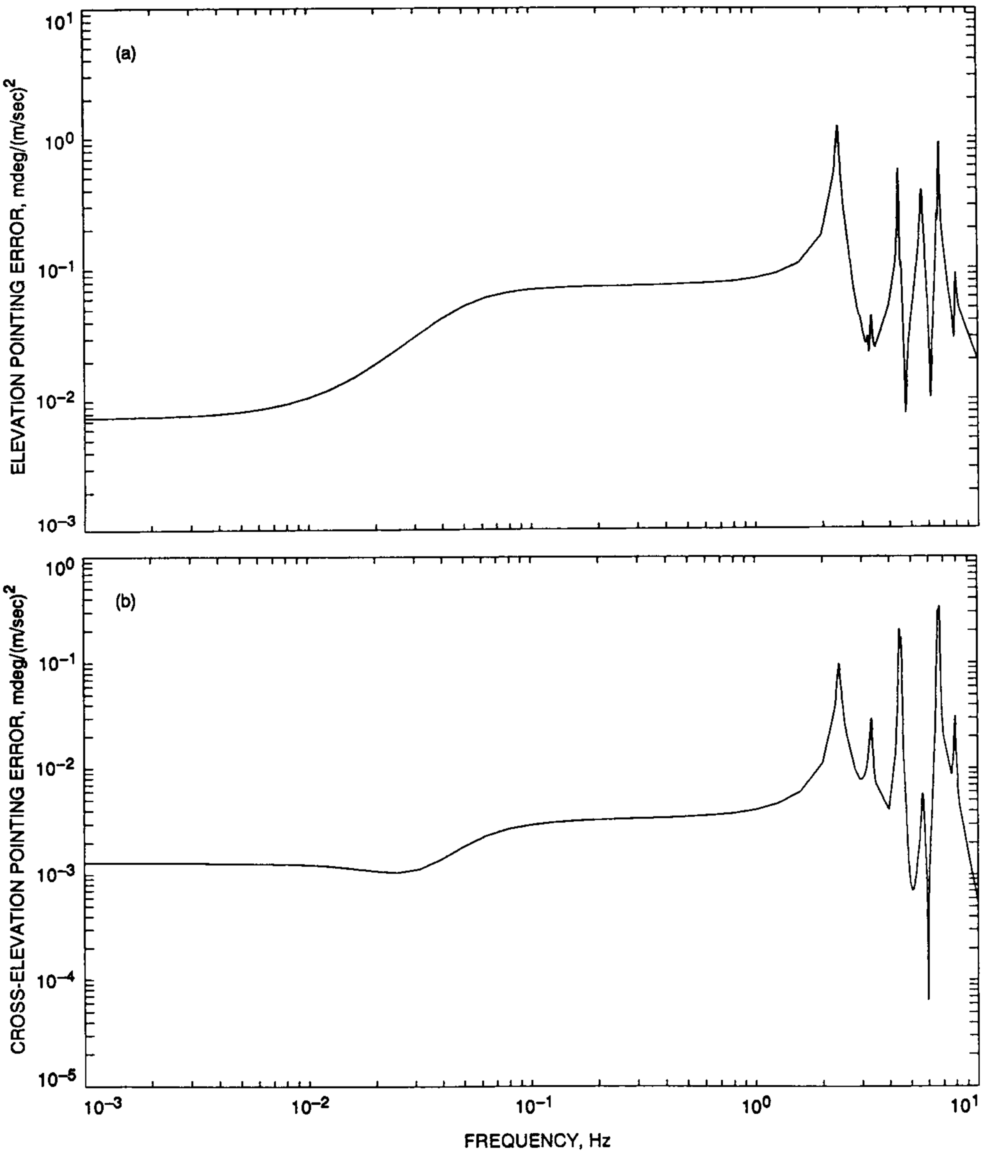

Fig. 12. Frequency-response functions for *y*-direction wind: (a) elevation pointing error and (b) cross-elevation pointing error.

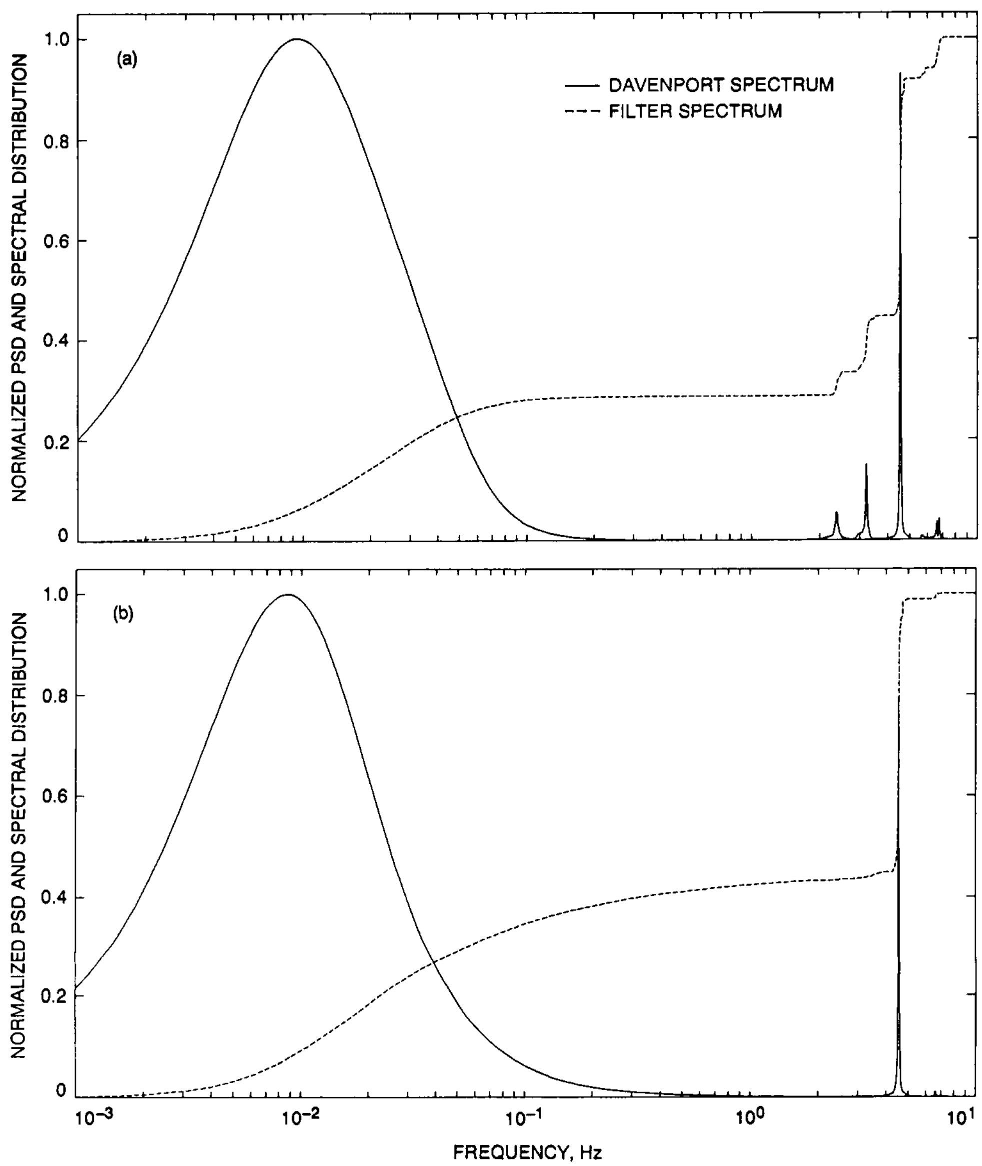

Fig. 13. Spectral density and spectral distribution functions for *x*-direction wind: (a) elevation pointing error and (b) cross-elevation pointing error.

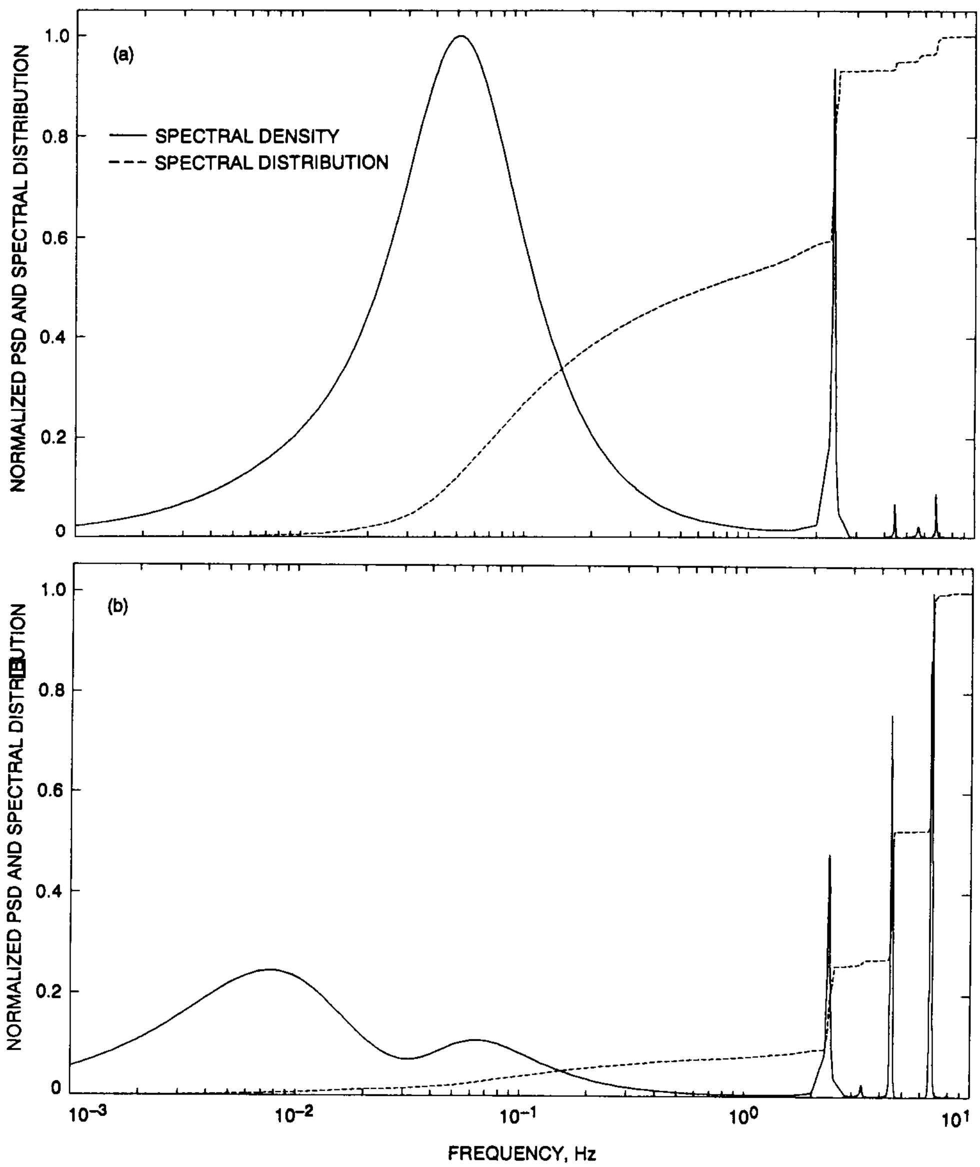

Fig. 14. Spectral density and spectral distribution functions for *y*-direction wind: (a) elevation pointing error and (b) cross-elevation pointing error.